

Effect of the Materials Properties of Hydroxyapatite Nanoparticles on Fibronectin Deposition and Conformation

Fei Wu,[†] Debra D. W. Lin,[†] Jin Ho Chang,[‡] Claudia Fischbach,^{‡,§} Lara A. Estroff,^{†,§} and Delphine Gourdon^{*,†,‡}

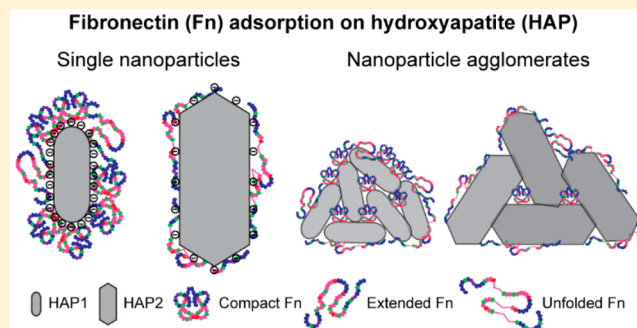
[†]Department of Materials Science and Engineering, Cornell University, Ithaca, New York 14853 United States

[‡]Department of Biomedical Engineering, Cornell University, Ithaca, New York 14853 United States

[§]Kavli Institute at Cornell for Nanoscale Science, Ithaca, New York 14853, United States

Supporting Information

ABSTRACT: Hydroxyapatite (HAP, $\text{Ca}_{10}(\text{PO}_4)_6(\text{OH})_2$) nanoparticles with controlled materials properties have been synthesized through a two-step hydrothermal aging method to investigate fibronectin (Fn) adsorption. Two distinct populations of HAP nanoparticles have been generated: HAP1 particles had smaller size, plate-like shape, lower crystallinity, and more negative ζ potential than HAP2 particles. We then developed two-dimensional platforms containing HAP and Fn and analyzed both the amount and the conformation of Fn via Förster resonance energy transfer (FRET) at various HAP concentrations. Our FRET analysis reveals that larger amounts of more compact Fn molecules were adsorbed onto HAP1 than onto HAP2 particles. Additionally, our data show that the amount of compact Fn adsorbed increased with increasing HAP concentration due to the formation of nanoparticle agglomerates. We propose that both the surface chemistry of single nanoparticles and the size and morphology of HAP agglomerates play significant roles in the interaction of Fn with HAP. Collectively, our findings suggest that the HAP-induced conformational changes of Fn, a critical mechanotransducer protein involved in the communication of cells with their environment, will ultimately affect downstream cellular behaviors. These results have important implications for our understanding of organic–inorganic interactions in physiological and pathological biominerization processes such as HAP-related inflammation.



INTRODUCTION

The adsorption of proteins onto surfaces is a common but complicated phenomenon in numerous biological processes and has promoted great research interest in various fields. For example, proteins adsorbed onto biomedical implants can trigger the complement cascade and cause inflammation.¹ In the biominerization community, it is widely acknowledged that protein–crystal interactions also play important roles in controlling crystal nucleation and growth.^{2–4} One biocompatible and bioactive material often used as implant coating for bone regeneration is hydroxyapatite (HAP, $\text{Ca}_{10}(\text{PO}_4)_6(\text{OH})_2$), which is closely related to bone apatite. Bone apatite, as compared with geologic HAP, has lower crystallinity and carbonate ions substituting for some fraction of hydroxyl and phosphate ions. Furthermore, the size, crystallinity, and compositional heterogeneity of bone apatite change as a function of age and disease progression.^{5–7} In this study, we focus on the interaction between HAP and fibronectin (Fn), a 440 kDa multimodular glycoprotein present both in soluble form (as single molecules) in the blood and in polymerized insoluble form (as macromolecular fibers) in the extracellular matrix (ECM).⁸ The HAP–Fn interface has received increasing

attention due to the ubiquitous role of mineral–protein interactions both in the design of biomedical implants and in the understanding of physiological/pathological processes such as wound healing/calcification. However, the molecular mechanisms of interactions between HAP and Fn remain unclear; in particular, the effect of materials properties of HAP on the quantity and conformation of adsorbed Fn is still not fully understood due to the intrinsic structural and chemical complexities of Fn.

The conformation and quantity of proteins adsorbed onto a surface depend on numerous factors, which include: surface chemistry, roughness, and local geometric characteristics such as curvature.^{9,10} Specifically, electrostatic forces play an important role in governing interactions between proteins and biominerals.¹¹ For example, experiments have shown that Fn adsorbs preferentially onto purely ionic crystal faces of calcite with no surface bound water molecules.¹² A previous study using Förster resonance energy transfer (FRET) and

Received: February 15, 2015

Revised: April 12, 2015

Published: April 14, 2015

atomic force microscopy (AFM) further demonstrates that local changes in the electrostatic environment during the growth of calcium oxalate monohydrate can induce major alterations in Fn conformation.¹³ Surface charge has been shown to regulate Fn conformation and integrin binding using model self-assembled monolayer substrates, where Fn molecules adsorbed onto negatively charged surfaces functionalized with carboxyl groups interact more strongly with $\alpha_5\beta_1$ integrins and induce efficient cellular adhesion as compared with Fn adsorbed onto neutral surfaces.¹⁴

With the rapid growth of nanotechnology over the years, engineered nanomaterials have been increasingly suggested for biomedical applications such as drug delivery and disease diagnosis. Thus, understanding interactions at the nanomaterial–biological interface becomes very important in designing safe biomaterials.¹⁵ Previous experimental work has shown that nanoroughness of substrates enhances protein adsorption and induces conformational changes of proteins, such as Fn.^{14,16} Additionally, local surface geometry of nanomaterials, such as curvature of nanoparticles and nanopores, can also significantly affect protein conformation, especially when the characteristic sizes of the nanomaterial and the protein are comparable.^{17,18} Therefore, both surface chemistry and morphology need to be carefully investigated when studying protein adsorption on nanomaterials.

Although a lot of effort has been devoted to studying HAP interactions with mineral-modulating proteins,³ there is still limited work on HAP–Fn interactions. Previous computational studies suggest that the adsorption of Fn-type III modules, either the single Fn-III₁₀ module or the Fn-III_{7–10} sequence, onto crystal faces of HAP is governed by electrostatic interactions and hydrogen bonds forming between the guanidine groups of arginine residues on Fn modules and the phosphate groups on HAP surface.^{19–21} Experimental studies have demonstrated that Fn molecules adsorbed onto smooth HAP surfaces show higher availability of the cell binding domain (Fn-III_{9–10}) and that cell spreading is enhanced as compared with Fn adsorbed onto smooth Au surfaces, possibly contributing to the biocompatibility of HAP implants.^{22,23} AFM force spectroscopy has revealed that Fn molecules adsorbed onto HAP surfaces require higher total unfolding force than Fn adsorbed onto atomically smooth mica surfaces, indicating that Fn may have stronger interactions with HAP than with mica.²⁴ Additionally, UV-vis spectrometry has shown that the crystallite size and specific surface area of HAP nanoparticles, together with protein bulk concentration, all affect the amount of Fn adsorbed.²⁵ However, the average conformation of Fn adsorbed onto HAP requires further investigation.

The HAP–Fn interface has important physiological and pathological relevance, as it resembles the apatite–ECM interface in bone microenvironments and the microcalcification–ECM interface in inflamed tissues including blood vessels and primary mammary tumors. The ECM is a fibrillar network composed mainly of collagen and Fn fibers and plays a vital role in regulating cellular responses to chemical and mechanical signals from the microenvironment.²⁶ We are particularly interested in Fn, as it is the first protein deposited by cells in the ECM, and as it regulates the deposition of other ECM components, such as collagen type I.^{27,28} Furthermore, Fn is dramatically upregulated during inflammation.²⁹ As a critical mechanotransducer, the force-induced conformational changes of Fn can regulate the type of binding sites that are exposed or disrupted, in particular the integrin binding sites located on Fn-

III_{9–10} used for cell attachment. More importantly, these conformational-dependent binding events ultimately influence downstream cellular behaviors to regulate or dysregulate homeostasis *in vivo*.^{30–32}

In this study, we have synthesized two distinct populations of HAP nanoparticles, HAP1 and HAP2, with controlled size, shape, and crystallinity. HAP1 is more physiologically relevant than HAP2, as it more closely resembles bone apatite in terms of size, shape, and crystallinity.⁵ It is worth noting that bone-derived HAP particles have been reported to show negative ζ potential, which promotes attachment and proliferation of bone cells.³³ By combining Fn and HAP nanoparticles at various HAP concentrations, we have investigated how the materials properties of HAP nanoparticles affect the amount and conformation of adsorbed Fn using FRET spectroscopy.^{30,34} Our results demonstrate that both the amount and the conformation of Fn are affected by (i) the size, crystallinity, and shape of single HAP nanoparticles, as well as by (ii) the size and morphology of nanoparticle agglomerates.

■ EXPERIMENTAL SECTION

HAP Nanoparticle Synthesis. HAP nanoparticles with controlled size, crystallinity, and shape were synthesized through a typical wet precipitation reaction of a calcium salt with a phosphate salt followed by hydrothermal treatment for 0 or 6 days.³⁵ All chemicals for these reactions were obtained from Sigma-Aldrich and used as received. A solution of $(\text{NH}_4)_2\text{HPO}_4$ (300 mL, 10 mM) was added dropwise into a solution of $\text{Ca}(\text{NO}_3)_2$ (500 mL, 10 mM) under rapid stirring at 4 °C in an ice–water bath for a final calcium to phosphate ratio of 1.67. The pH of the starting solution was adjusted to pH 10 with 0.1 M NH_4OH . The reaction was allowed to proceed for 1 h at 4 °C and then stirred at 20 °C for 3 days. After 3 days, the resulting opaque suspension was divided into 720 mL for concentration and 80 mL for further reaction. The 720 mL opaque suspension was allowed to settle until separation of white sediment from clear supernatant; after decanting the clear supernatant, the concentrated suspension (100 mL) was used to obtain HAP1 nanoparticles. The remaining 80 mL of the original opaque suspension was placed in a pressure vessel (Parr Instrument Company 4748) and heated at 180 °C in an oven for 6 days to obtain HAP2 nanoparticles. The nanoparticle suspensions were then transferred into a regenerated cellulose tubular membrane (Cellu-Sep T1 5030-46, Nominal MWCO 3500) and dialyzed against 1× phosphate buffered saline (PBS) at pH 7.4 for 5 days. After dialysis, the nanoparticle suspensions were further concentrated by decanting the clear supernatant as described previously and stored in glass vials as stock solutions. To determine the concentration of nanoparticles in PBS, a known volume of the stock solution was concentrated by centrifugation (Thermo Scientific Sorvall Legend RT + Centrifuge, 3600g, 7 min), washed with 0.15 M NH_4OH twice, rinsed with acetone, and dried at 20 °C. The dried nanoparticles were then weighed to obtain concentration of the stock solution and used for characterization.

HAP Nanoparticles Characterization. Powder X-ray diffraction (pXRD) was used to determine particle phase. Fourier transform infrared spectroscopy (FTIR) was used to assess the crystallinity of the nanoparticles. The size and shape distributions of the nanoparticles were determined by transmission electron microscopy (TEM). Zeta potential of the nanoparticles was measured using laser doppler electrophoresis (LDE). Dried nanoparticles were examined by pXRD (Scintag Inc. PAD-X theta–theta X-ray diffractometer, Cu K α 1.54 Å, accelerating voltage 40 kV, current 40 mA, continuous scan, 1.0 deg/min). Scherrer analysis was used to determine crystalline domain sizes from the peak broadening of the {002} peak of HAP (25.88°) using an Al_2O_3 standard to correct for instrumental broadening (software: JADE 9, Materials Data, Inc.). For FTIR (Mattson Instruments 2020 Galaxy Series FT-IR), dried particles were used to prepare KBr pellets and to acquire spectra (res 4.0 cm⁻¹, 256 scans). Particle crystallinities

were determined from the splitting factor obtained via normalizing the sum of the absorbance at 565 and 603 cm⁻¹ to the minimum between the doublet following Weiner and Bar-Yosef.³⁶ For TEM, a stock solution of dialyzed particles in PBS was diluted with PBS and dropped onto a carbon-coated copper TEM grid (Electron Microscopy Sciences). After 10 min, PBS was wicked away with filter paper and the sample was left to dry for another 10 min. Bright field TEM (FEI Tecnai T-12 Spirit, 120 kV) images were analyzed through ImageJ (NIH) to determine the size and shape of particles. For ζ potential measurements, HAP stock solutions were diluted to various concentrations in PBS and measured in folded capillary cells using Zetasizer Nano-ZS (Malvern Instruments Ltd. ZEN3600), with 3–6 measurements and a total of 20–30 runs per sample.

Fibronectin and FRET Labeling. Fibronectin (Fn) was obtained from Life Technologies, NY. AlexaFluor 488 succinimidyl ester and AlexaFluor 546 maleimide (Invitrogen, CA) were used to label Fn for intramolecular FRET as previously described by Baneyx et al.³⁴ and Smith et al.³⁰ Labeling ratios and Fn concentrations were determined using a DU730 UV/vis spectrophotometer (Beckman, IN) at 280, 495, and 556 nm. Soluble calibration of FRET labeled Fn was carried out in guanidine hydrochloride (GdnHCl) solution at concentrations of 0, 2, and 4 M to obtain FRET ratios, defined as acceptor/donor intensity ratios (I_A/I_D) as a function of protein denaturation.

Fabrication of Two-Dimensional Platforms. Two-dimensional platforms were fabricated using 8-well Lab-Tek chambers with borosilicate coverglass bottom (Thermo Fisher Scientific Inc.). Dialyzed nanoparticles in PBS were used to dilute stock solutions of Fn to 50 μ g/mL. The diluted Fn solution contains 10% FRET labeled Fn and 90% unlabeled Fn to avoid intermolecular FRET, so that only intramolecular FRET was measured to assess conformation of single Fn molecules.³⁰ After mixing, the concentrations of the nanoparticles were 0.01, 0.05, and 0.1 mg/mL, while the concentration of Fn was kept to 50 μ g/mL for all conditions. Then 130 μ L of the mixture was added to each well and incubated at 4 °C for 24 h before imaging.

FRET Data Acquisition. Two-dimensional platforms containing HAP and Fn were imaged with a Zeiss 710 confocal microscope (Zeiss, Munich, Germany). 16-bit z-stack images were acquired using the C-Apochromat water-immersion 40 \times /1.2 objective, a pinhole of 1 AU, 488 nm laser with 30% laser power, pixel dwell time of 6.3 μ s, PMT1 and PMT2 gains of 600 V, and z step size of 0.5 μ m. FRET labeled Fn molecules were excited with a 488 nm laser line; emissions from donor and acceptor fluorophores were simultaneously collected in the PMT1 channel (514–526 nm) and the PMT2 channel (566–578 nm), respectively. Meanwhile transmitted light images were acquired in the T-PMT channel (transmitted light detector). These z-stack images were analyzed with a customized Matlab code to generate FRET ratio (I_A/I_D) images and histograms, as well as mean FRET ratios for all z-slices in a z-stack.

Statistical Analysis. One-way ANOVA with Tukey's post test and Student's *t* test were used to determine statistical significance between conditions in GraphPad Prism (GraphPad Software, Inc., CA). In all cases, *p* < 0.05 is indicated by a single asterisk, *p* < 0.01 by two asterisks, and *p* < 0.001 by three asterisks.

RESULTS

HAP Nanoparticles Characterization. HAP nanoparticles were synthesized through a wet precipitation reaction of Ca(NO₃)₂ with (NH₄)₂HPO₄ at low temperature. HAP1 particles were isolated directly and then dialyzed against PBS. HAP2 particles were formed by further hydrothermal treatment of the precipitate for 6 days followed by dialysis. Both HAP1 and HAP2 were confirmed to be pure HAP by pXRD (Figure S1A, Supporting Information). Domain sizes along the *c*-axis of the nanoparticles were determined from Scherrer analysis of the {002} peak of HAP (25.88°) to be 24 ± 2 nm for HAP1 and 65 ± 7 nm for HAP2 (Table 1). The pXRD pattern of HAP2 showed more clearly resolvable peaks at higher angles as

Table 1. Summary of Hydrothermal Treatment Time, Sizes, and Splitting Factors of the Nanoparticles

ID	hydrothermal treatment time [d]	domain size along <i>c</i> -axis [nm] (pXRD) ^a	particle size along <i>c</i> -axis [nm] (TEM) ^b	splitting factor (FTIR) ^c
HAP1	0	24 ± 2	32 ± 8	3.95
HAP2	6	65 ± 7	67 ± 25	6.97

^aDomain sizes of the particles along *c*-axis were determined from pXRD by Scherrer analysis of the {002} peak. ^bParticle sizes along *c*-axis obtained from TEM were presented as means with standard deviations. ^cSplitting factors were obtained from FTIR spectra by normalizing the sum of the absorbance at 565 and 603 cm⁻¹ from PO₄ bond bending to the minima between the two peaks.

compared with HAP1 particles, suggesting an increase in crystallinity after hydrothermal treatment.

FTIR spectra were acquired to confirm the increase in crystallinity of HAP2 particles after hydrothermal treatment (Figure S1B, Supporting Information). The absorbance at 635 cm⁻¹ is attributed to structural hydroxides in HAP and is known to increase with enhanced crystallinity.³⁷ This absorbance was undetectable for HAP1, and increased in intensity for HAP2, confirming an increase in crystallinity of particles after hydrothermal treatment. Finally, the splitting factor quantifies the degree of splitting of the PO₄ bond bending peaks (565 and 603 cm⁻¹) and is known to increase with increasing crystallinity.³⁶ HAP2 had a larger splitting factor than HAP1, as further confirmation of higher crystallinity (Table 1).

The shape and size distributions of particles were determined by TEM (Figure 1). Both HAP1 and HAP2 were elongated along the *c*-axis. HAP1 (Figure 1A) had a plate-like shape with an average length of 32 ± 8 nm (*N* = 213) along the *c*-axis; HAP2 (Figure 1B) had the shape of a hexagonal prism with an average length of 67 ± 25 nm (*N* = 688) along the *c*-axis (Table 1). Both HAP1 and HAP2 had narrow size distributions (Figure S2, Supporting Information).

In addition to physical and structural properties, we also characterized the surface chemical properties of the nanoparticles by measuring ζ potential. Zeta potential of the particles at various concentrations was measured in PBS at pH 7.4 (Figure 2). Both HAP1 and HAP2 had negative ζ potential. At all concentrations, HAP1 had more negative ζ potential than HAP2. Moreover, the magnitude of the ζ potential decreased with increasing HAP concentration for both HAP1 and HAP2.

Collectively, our characterization data indicate that we have two distinct populations of HAP particles, HAP1 and HAP2. Moreover, our ζ potential results suggest that the size and morphology of HAP agglomerates evolve with increasing HAP concentration. We next assessed the effects of the materials properties of these nanoparticles on their interaction with Fn by investigating Fn adsorption at various HAP concentrations.

Fn Deposition and Conformation at Various HAP Concentrations. To investigate whether HAP materials properties affect their interaction with Fn, confocal images of two-dimensional platforms containing HAP nanoparticles and Fn were acquired to quantify both the amount and the conformation of Fn adsorbed onto HAP at various HAP concentrations. A diluted Fn solution (50 μ g/mL, 10% FRET labeled) was used for incubation to ensure that only intramolecular FRET was measured to assess conformation of single Fn molecules.³⁰ Donor and acceptor fluorophores were imaged simultaneously (Figure 3A,B), along with a bright-field

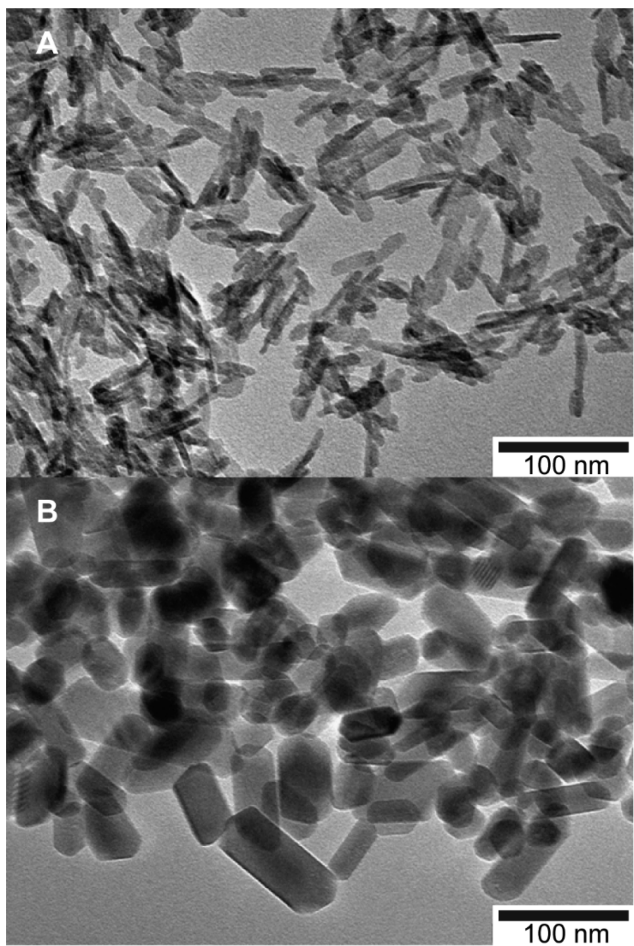


Figure 1. TEM images of HAP nanoparticles synthesized through a wet precipitation method after dialysis: (A) HAP1, (B) HAP2 (hydrothermal treatment for 6 days).

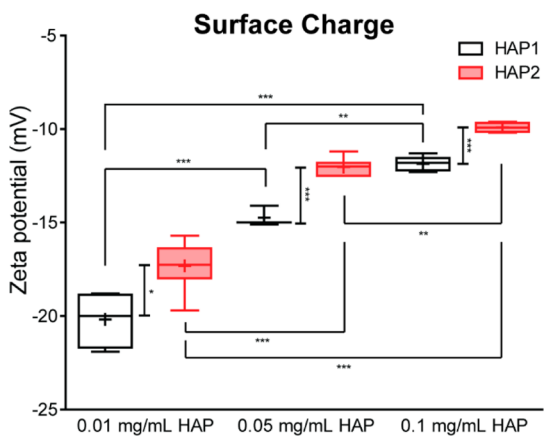


Figure 2. Zeta potential of HAP nanoparticles at various concentrations in PBS. Data collected from 3–6 measurements and a total of 20–30 runs per sample. In all cases, $p < 0.05$ is indicated by a single asterisk, $p < 0.01$ by two asterisks, and $p < 0.001$ by three asterisks.

image recorded in the transmission light channel (Figure 3C) for each field of view. FRET ratio was defined as acceptor/donor intensity ratio (I_A/I_D). The color-coded FRET ratio map and FRET ratio histogram were used to calculate mean FRET ratio for each field of view (Figure 3D,E). As determined in our

FRET calibration (Figure S3, Supporting Information), together with previously published circular dichroism data,³⁰ FRET ratio is high when Fn has a compact conformation (0 M GdnHCl), decreases as Fn opens up and becomes extended (0–2 M GdnHCl), and further decreases when Fn starts losing tertiary structure (2–4 M GdnHCl), i.e., when Fn type-III modules (magenta ovals/lines in Figure 3E schematics) start unfolding.

We first used FRET to determine the conformation of Fn adsorbed onto HAP nanoparticles at various concentrations (Figure 4A). Fn adsorbed onto HAP1 particles had systematically higher FRET ratios than Fn adsorbed onto HAP2 particles at all HAP concentrations. These data suggest that, on average, Fn molecules were more compact when adsorbed onto HAP1 than onto HAP2. Additionally, FRET ratios increased with increasing HAP concentration for both HAP1 and HAP2 particles, indicating that Fn molecules overall adopted more compact conformations as HAP concentration increased. Borosilicate coverglass and freshly cleaved mica were used as control surfaces: FRET ratios of Fn adsorbed onto coverglass and mica were 0.642 ± 0.008 and 0.494 ± 0.007 , respectively (data reported as mean \pm standard deviation), suggesting that Fn unfolding increased slightly upon adsorption onto coverglass and drastically upon adsorption onto atomically smooth mica, as compared with HAP.

We next quantified the amount of Fn adsorbed per unit volume onto HAP particles by monitoring the sum of donor and acceptor fluorescence intensities (Figure 4B). The sum of donor and acceptor fluorescence intensities was larger for HAP1 particles at all concentrations, suggesting that there were systematically more Fn adsorbed onto HAP1 than onto HAP2 particles. Furthermore, the amount of Fn adsorbed onto HAP2 particles increased with increasing HAP concentration, whereas the amount of Fn adsorbed onto HAP1 particles reached a plateau at high (0.1 mg/mL) HAP concentration. The sums of donor and acceptor fluorescence intensities of Fn adsorbed onto coverglass and mica were 358 ± 8 and 221 ± 12 , respectively (data reported as mean \pm standard deviation, $N = 8$), suggesting that more Fn was adsorbed onto coverglass than onto mica. In addition, the sums for both coverglass and mica were lower than those for HAP nanoparticles at all concentrations, suggesting that Fn adsorption was enhanced for HAP nanoparticles. Collectively, our data show that (i) larger amounts of more compact Fn molecules adsorbed onto HAP1 as compared with HAP2 particles, and (ii) more compact Fn also tended to adsorb with increasing HAP concentration until the total amount of molecules adsorbed onto HAP reached a plateau.

Size and Morphology of HAP Nanoparticle Agglomerates. The acceptor channels of z-stack confocal images of Fn adsorbed onto HAP nanoparticles were used to generate three-dimensional reconstruction of nanoparticle agglomerates to analyze the size, number, and morphology of the agglomerates (Figures 5 and 6). Both HAP1 and HAP2 particles formed microscale agglomerates in PBS. At low HAP concentration (0.01 mg/mL), the sizes of agglomerates were typically below 10 μm (Figures 5A and 6A). The fluorescence intensity is proportional to the amount of Fn adsorbed per unit volume; hence, the low fluorescence intensity detected at low HAP concentration suggests that only a small amount of Fn molecules was adsorbed onto the surface of nanoparticles that were assembled in a few small agglomerates. At higher HAP concentration (0.05 mg/mL), both the number and size

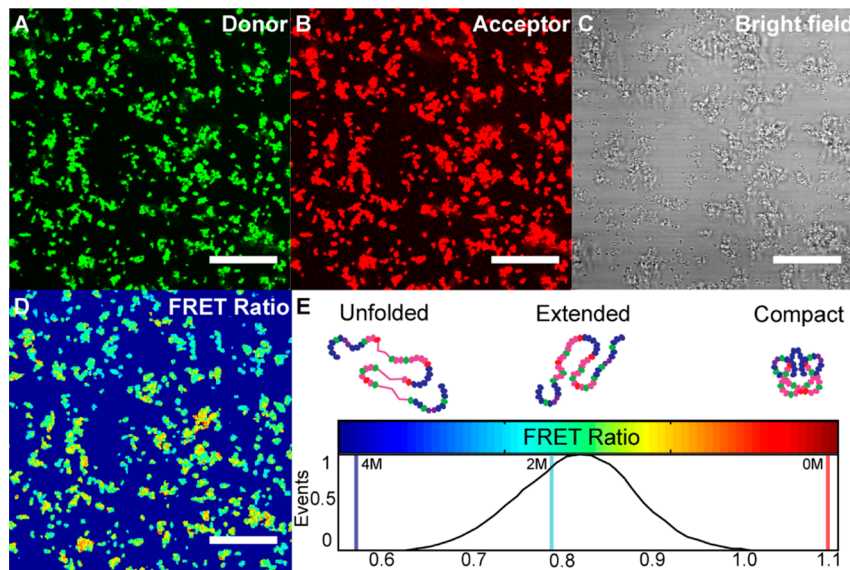


Figure 3. Confocal images for 0.05 mg/mL HAP1 nanoparticles incubated with Fn: (A) Donor channel, (B) acceptor channel, and (C) transmission light channel. (D) Color-coded FRET ratio map, with high FRET ratio color coded in red (compact Fn) and low FRET ratio in blue (unfolded Fn). (E) FRET ratio histogram for the same field of view, with schematics of Fn conformation correlated to the FRET calibration values reported in Figure S3, Supporting Information (compact, loss of quaternary structure when extended, and loss of tertiary structure when type-III modules represented by magenta ovals/lines start unfolding).³⁰ Scale bars 50 μ m.

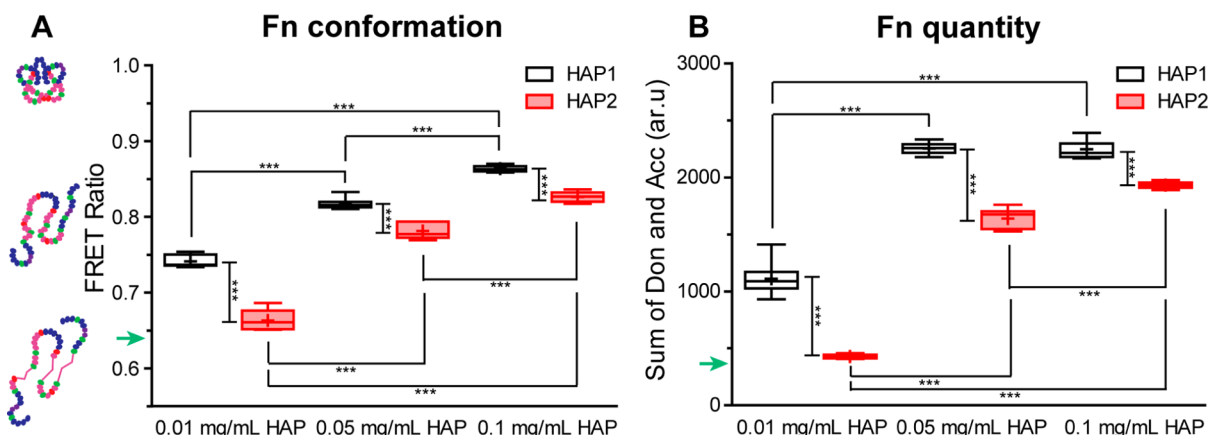


Figure 4. (A) FRET ratio and (B) amount of Fn adsorbed onto HAP1 and HAP2 at various HAP concentrations, after incubation at 4 °C for 24 h. All data shown were obtained from the z slice 2 μ m above the bottom coverglass, with 5–8 fields of view analyzed per sample. As a comparison, FRET ratio and quantity of Fn adsorbed onto coverglass (in absence of HAP) are indicated by green arrows in (A) and (B), respectively. All sample conditions were repeated three times. In all cases, $p < 0.05$ is indicated by a single asterisk, $p < 0.01$ by two asterisks, and $p < 0.001$ by three asterisks.

of agglomerates increased, reaching up to 35 μ m in height (Figures 5B and 6B). The higher fluorescence intensity also suggests that more Fn molecules were adsorbed. Finally at 0.1 mg/mL, the size of agglomerates displayed a wide distribution, ranging from several μ m to 50 μ m in height (Figures 5C and 6C). To exclude FRET signal from Fn adsorbed onto the bottom coverglass, we discarded the slice $z = 0$ and used the slice $z = 2 \mu$ m (above the coverglass) to quantify Fn conformation and quantity adsorbed at various HAP concentrations (Figure 4).

When comparing the size and morphology of HAP1 and HAP2 agglomerates, they appeared to be similar at the same concentration (Figures 5 and 6). However, the fluorescence intensity of Fn was lower on HAP2 particles, confirming that less Fn molecules were adsorbed onto HAP2 than onto HAP1 particles (at equal HAP concentration), which is in agreement with results presented in Figure 4.

■ DISCUSSION

This study demonstrates that the size, shape, and crystallinity of single HAP nanoparticles as well as particle agglomeration collectively affect both the amount and the conformation of Fn adsorbed onto HAP. Two distinctive populations of HAP nanoparticles have been used, with HAP1 particles having smaller size, plate-like shape, lower crystallinity, and more negative ζ potential than HAP2 particles. Our results show that larger amounts of more compact Fn were adsorbed onto HAP1, while smaller amounts of more extended and unfolded Fn were found on HAP2. Additionally, increased adsorption of more compact Fn was observed at higher HAP concentration, when large agglomerates were more prone to form. We thus propose that both the surface chemistry of single HAP nanoparticles and the size and morphology of HAP agglomerates contribute significantly to Fn–HAP interactions in PBS.

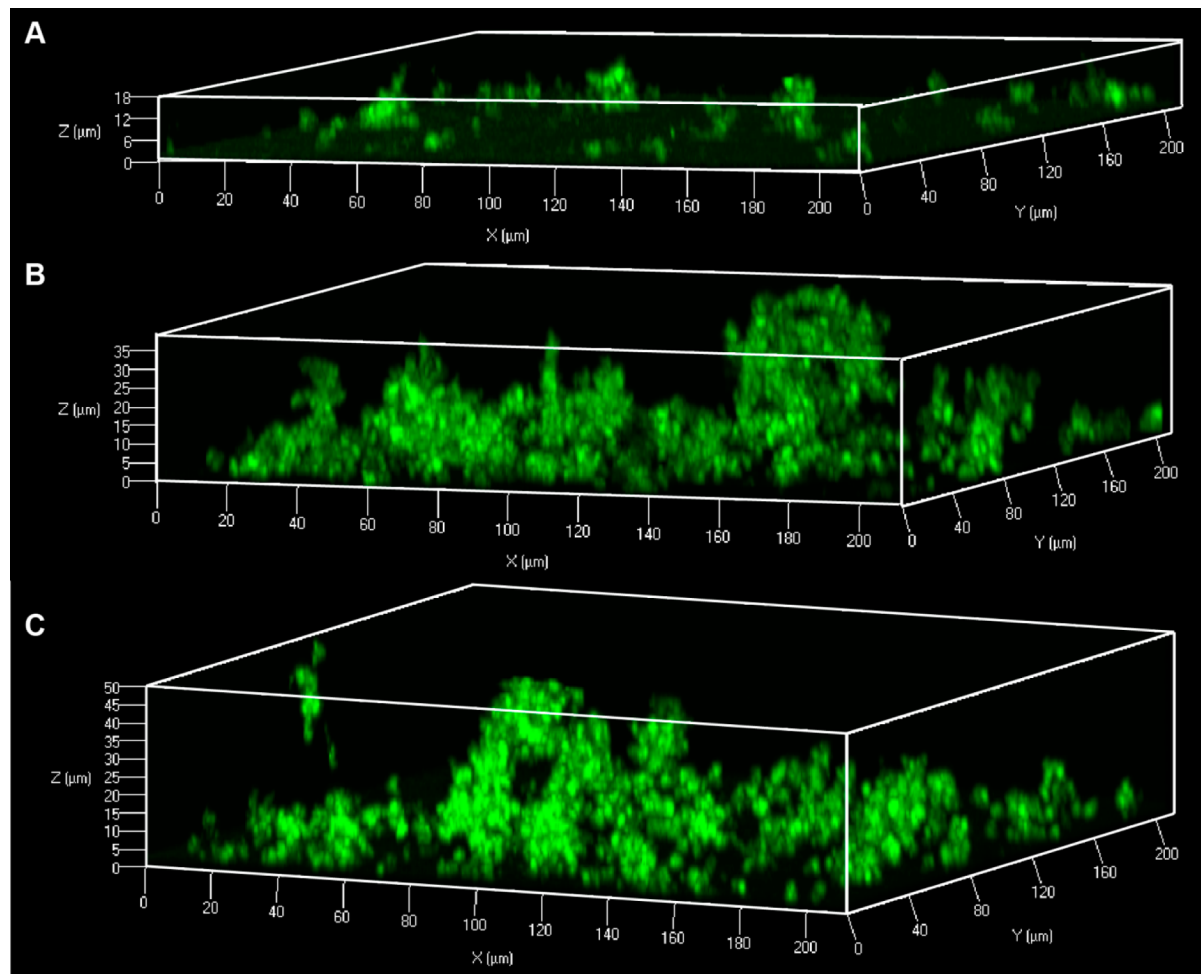


Figure 5. Confocal z-stack three-dimensional reconstruction: size and morphology of HAP1 nanoparticle agglomerates at (A) 0.01 mg/mL, (B) 0.05 mg/mL, and (C) 0.1 mg/mL incubated with Fn in PBS.

Effect of HAP Nanoparticle Surface Chemistry on Fn Adsorption. The more compact conformation of Fn adsorbed onto HAP1 compared with HAP2 particles is attributed to HAP surface chemistry, which directly controls electrostatic interactions between single HAP particles and Fn in PBS (Figure 7A). In support of this proposal, there have been computational studies suggesting that the adsorption of acidic proteins such as osteopontin to the (100) face and Fn-III₁₀ peptides to the (001) face of HAP is governed by electrostatics.^{19,20} Given that our HAP nanoparticles are elongated along the *c*-axis, and that the (100) face has been shown to be the most favorable energetically in water,³⁸ we speculate that the largest surface of our HAP nanoparticles is probably the (100) face. Among the two types of HAP nanoparticles, HAP1 particles with smaller size, plate-like shape and lower crystallinity show more negative ζ potential at all concentrations (Figure 2). The more negative ζ potential of HAP1 particles likely implies denser surface charge and thus stronger electrostatic interactions with Fn. Although Fn has an acidic isoelectric point,³⁹ hence a net negative charge at pH 7.4, its numerous positively charged residues can readily interact with HAP surfaces through electrostatic interactions or hydrogen bonding.

The larger amount of Fn adsorbed onto HAP1 particles as compared with HAP2 particles is in agreement with previous work showing a decrease in Fn adsorption with increasing size

of HAP nanoparticles.²⁵ Adsorption of serum proteins has also been found to increase on polymer scaffolds containing smaller and less crystalline HAP nanoparticles.³⁵ It should be noted that our results in Figure 4B indicate the amount of Fn adsorbed per unit volume and may not be relevant to Fn adsorbed per unit surface area onto the nanoparticles. Each voxel ($0.4 \times 0.4 \times 1.0 \mu\text{m}^3$) can accommodate approximately 10K of HAP1 or 1K of HAP2 nanoparticles (assuming reasonable thickness). Additionally, single HAP1 particles have higher surface area to volume ratios than single HAP2 particles. Thus, the higher level of fluorescence measured for HAP1 compared to HAP2 could result from both the larger quantity and larger surface area of HAP1 particles per voxel, even if the same amount of Fn adsorbed per unit surface area onto HAP1 and HAP2 particles. However, our FRET results in Figure 4A suggest that Fn adopts a more compact conformation and hence takes less space when adsorbed onto HAP1, implying that there could be more Fn adsorbed per unit surface area on HAP1 compared to HAP2.

Moreover, we observe a correlation between the quantity and the conformation of Fn adsorbed, with larger Fn amounts correlating systematically to more compact Fn conformations. This correlation can be attributed either to a reduced space available for each Fn molecule adsorbed or to protein–protein interactions that stabilize compact Fn conformation at high surface coverage (in particular on HAP1 surface). Our data are

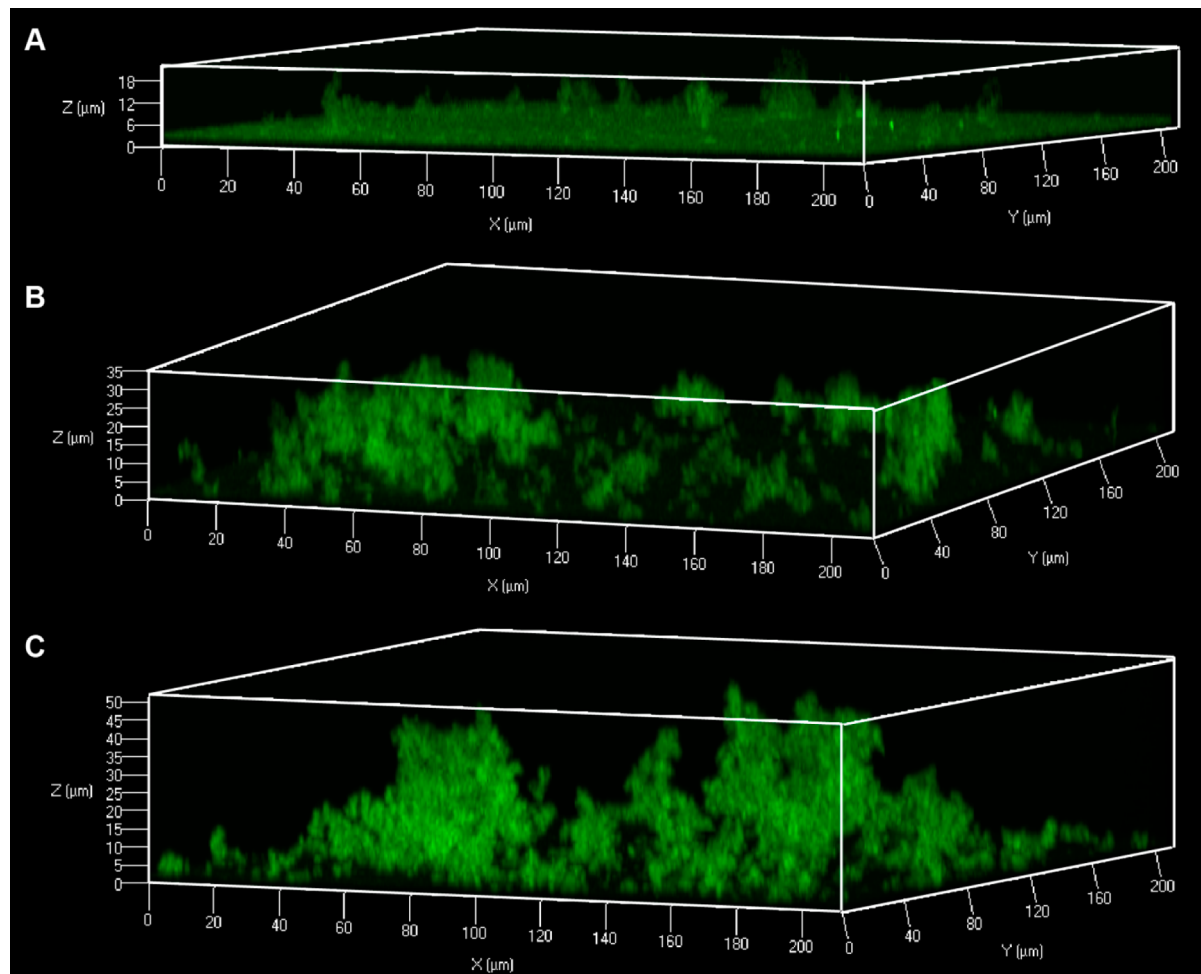


Figure 6. Confocal z-stack three-dimensional reconstruction: size and morphology of HAP2 nanoparticle agglomerates at (A) 0.01 mg/mL, (B) 0.05 mg/mL, and (C) 0.1 mg/mL incubated with Fn in PBS.

in agreement with previous work reporting a similar relationship between the interfacial concentration and conformation of Fn adsorbed onto hydrophobic polystyrene, in which the authors suggested that molecular packing and protein–protein interactions at high Fn bulk concentration reduced Fn molecular unfolding.⁴⁰ On hydrophilic surfaces, such as mica, the orientation and conformation of Fn have been shown to depend on surface coverage as well, where increasing specific interactions with collagen-related peptides is observed at higher surface coverage.⁴¹ In fact, our FRET results show that Fn molecules adsorbed onto atomically smooth mica at very low bulk concentration (50 μg/mL) are mostly unfolded.

Evolving Size and Morphology of HAP Agglomerates with Increasing HAP Concentration. The stability of a colloidal system can be indicated by the magnitude of the ζ potential. Previous work has shown that a smaller magnitude of ζ potential indicates weaker electrostatic repulsion between nanoparticles and hence promotes the formation of agglomerates.⁴² Our ζ potential results suggest that the size and morphology of HAP agglomerates evolve with increasing HAP concentration (Figure 2), as further confirmed by our three-dimensional reconstruction of z-stack confocal images (Figures 5 and 6). According to Figures 5 and 6, the morphology of HAP agglomerates is fractal-like and heterogeneous in both size and shape, as observed for other colloidal systems.^{43,44} Although the size of agglomerates is widely distributed, larger

agglomerates are more likely to form at higher HAP concentration, as suggested by the decrease in the magnitude of the ζ potential.

Effect of HAP Agglomerate Size and Morphology on Fn Adsorption. We attribute the more compact conformation of Fn detected at higher HAP concentration to the varying size and morphology of HAP agglomerates (Figure 7B). At higher HAP concentration, the magnitude of the ζ potential of agglomerates decreases, implying that surface chemistry and electrostatic interactions might play less central roles in the overall Fn adsorption onto and within HAP agglomerates. Instead, the size and morphology of HAP agglomerates could be the dominant factors. Given that larger amounts of more compact Fn were measured at higher HAP concentration, i.e., when large agglomerates are more prone to form, we speculate that the enhanced Fn adsorption and stabilization of compact conformation correlate to the formation of large HAP agglomerates.

We further suggest that the numerous interstitial sites between HAP nanoparticles in large agglomerates are responsible for confining most Fn molecules in compact conformation within the bulk of agglomerates (Figure 7B). In support of this proposal, a previous study has demonstrated the stabilization of protein conformation within nanopores having an optimal size due to favorable confinement.¹⁷ As the surface to volume ratio is proportional to $1/R$ (assuming spherical

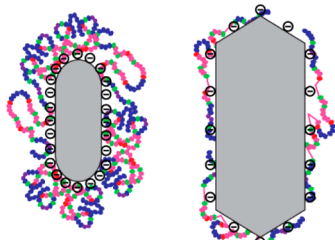
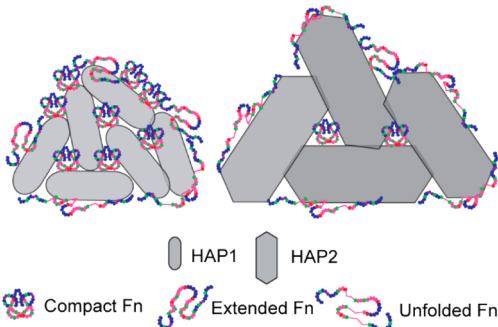
A Effect of HAP surface chemistry**B Effect of HAP agglomerate size and morphology**

Figure 7. Effect of HAP materials properties on Fn adsorption. (A) At low HAP concentration, denser surface charge of HAP1 (more negative ζ potential than HAP2) resulted in larger amounts of more compact Fn adsorbed onto the HAP1 surface. (B) At high HAP concentration, i.e., in the presence of large HAP agglomerates, numerous Fn molecules are confined (in compact conformation) within the interstitial sites between nanoparticles, which outweigh the number of molecules adsorbed onto the surface of the agglomerates (in extended/unfolded conformation). The ratio of surface-Fn to confined-Fn decreases with increasing agglomerate size, resulting in overall larger amounts of more compact Fn adsorbed at higher HAP concentration.

agglomerates, R being the radius), the ratio of surface-Fn to confined-Fn decreases with increasing agglomerate size. Therefore, the FRET signal detected at high HAP concentration comes mostly from confined-Fn (more compact) trapped within the volume of large agglomerates rather than from surface-Fn (more extended/unfolded). Although the exact size and shape of the interstitial sites between HAP nanoparticles are not known, increasing HAP concentration might result in smaller interstitial sites with dimensions comparable to the characteristic size of compact Fn, which is around 20 nm.³⁹ Alternatively, the local electrostatic environment within the interstitial sites, such as ionic strength, might also induce conformational changes of Fn.

Consistently, the more compact conformation of Fn detected at higher HAP concentration again correlates to higher amounts of Fn adsorbed, as previously discussed (Figure 4). However, in the case of HAP1, the quantity of Fn measured per unit volume reached a plateau at high HAP concentration (0.1 mg/mL). The plateau does not necessarily indicate monolayer coverage, as Fn molecules could also be trapped between nanoparticles within agglomerates even if the HAP surface is saturated with a monolayer of Fn. One possible explanation is that at 0.1 mg/mL of HAP1, there was a lack of available Fn molecules in the initial solution because of the very low bulk concentration (50 μ g/mL).

Our two-dimensional platforms containing Fn adsorbed onto HAP nanoparticles provide a reliable tool to control the conformation of proteins by tuning the materials properties of nanoparticles onto which they are adsorbed. The materials properties of HAP nanoparticles, including size, shape, crystallinity, and ζ potential, together with the conformation and amount of Fn adsorbed, have been well characterized. Thus, these platforms are ready to be exploited for investigating cellular behaviors such as cell adhesion, secretion, and migration as a function of Fn conformation and mineral materials properties. For example, our HAP1 particles closely resemble bone apatite in terms of size, shape, crystallinity, and surface chemistry (negative ζ potential) and hence can be used for studying bone remodeling and cancer metastasis to bone.^{5,33} In fact, the nanoscale materials properties of HAP have been shown to affect breast tumor cell adhesion, growth, secretion, and migration.^{35,45} In addition, HAP has been found in inflammation-associated calcifications whereby the materials properties of HAP change as a function of disease progression.^{46,47}

We anticipate that the HAP-induced conformational changes of Fn will regulate several cell functions by modulating the type of binding sites that will be exposed or disrupted on Fn, in particular the integrin binding sites located on Fn-III_{9–10} used for cell attachment. Work by Boettiger et al. has shown that cell adhesion strength increases with surface density of Fn;⁴⁸ moreover, conformational changes of surface-bound Fn modulate integrin binding and control cell signaling such as proliferation and differentiation.^{49,50} Additionally, our recent studies also indicate that unfolding of Fn decreases cell adhesion while enhancing secretion of vascular endothelial growth factor by preadipocytes in both 2D⁵¹ and 3D⁵² environments due to the favored use of $\alpha_5\beta_3$ (strain-insensitive) over $\alpha_5\beta_1$ (strain-sensitive) integrins when cells interact with Fn. In the current study, the lower surface density and more unfolded conformation of Fn adsorbed onto HAP2 are expected to lead to similar cell behaviors, i.e., decreased cell adhesion and enhanced secretion of growth factors. In such a context, our platforms can help us elucidate how HAP materials properties affect not only the biological function of Fn but also subsequent cell behaviors, providing insights into biological processes such as bone healing, osteoporosis, cancer metastasis to bone, and HAP-related inflammation.^{46,47,53,54}

CONCLUSIONS

We have combined nanoparticle synthesis with FRET spectroscopy to quantify the deposition and conformation of Fn adsorbed onto HAP nanoparticles with various materials properties. Our data reveal that larger amounts of more compact Fn molecules adsorb onto HAP nanoparticles with smaller size, lower crystallinity, and more negative ζ potential (resembling bone apatite). Additionally, we report a systematic increase in the adsorption of compact Fn molecules with increasing HAP concentration, attributed to the formation of larger HAP agglomerates. Collectively, our findings suggest that both the surface chemistry of single HAP nanoparticles and the size and morphology of HAP agglomerates contribute to Fn adsorption. Using our two-dimensional HAP–Fn platforms, further studies of the role of Fn conformation in regulating subsequent cellular behavior, such as cell adhesion and growth factors secretion, will provide important insights into a wide range of physiological and pathological processes involving HAP–cell interactions.

■ ASSOCIATED CONTENT

Supporting Information

pXRD pattern of nanoparticles. FTIR spectra of HAP nanoparticles. Size distributions along *c*-axis of HAP1 and HAP2 nanoparticles (TEM). Soluble calibration of FRET ratio (i.e., acceptor intensity/donor intensity) as a function of chemical denaturant (guanidine hydrochloride, GdnHCl) concentration. This material is available free of charge via the Internet at <http://pubs.acs.org>.

■ AUTHOR INFORMATION

Corresponding Author

*Phone: (607)255-1623. Fax: (607)255-2365. E-mail: dg434@cornell.edu. Address: Department of Materials Science and Engineering, Cornell University, 327 Bard Hall, Ithaca, New York 14853, United States.

Notes

The authors declare no competing financial interest.

■ ACKNOWLEDGMENTS

This work was funded by NSF under award DMR-1352299 (D.G.) and NIH/NCI under award R01 CA173083 (C.F. and L.A.E.). This research made use of the Nanobiotechnology Center shared research facilities at Cornell (NBTC) and the Cornell Center for Materials Research shared facilities (CCMR) supported through the NSF MRSEC program (NSF DMR-1120296). This work was also supported by the Cornell University Biotechnology Resource Center (BRC) Imaging Facility for data collected on the Zeiss LSM 710 Confocal (NIH 1S10RR025502-01). F.W. thanks Karin Wang for help with FRET labeling and FRET calibration.

■ REFERENCES

- (1) Kaplan, A. P.; Joseph, K.; Silverberg, M. *J. Allergy Clin. Immunol.* **2002**, *109*, 195–209.
- (2) De Yoreo, J. J.; Dove, P. M. *Science* **2004**, *306*, 1301–1302.
- (3) George, A.; Veis, A. *Chem. Rev.* **2008**, *108*, 4670–4693.
- (4) Hunter, G.; Goldberg, H. *Biochem. J.* **1994**, *302*, 175–179.
- (5) Hanschin, R. G.; Stern, W. B. *Bone* **1995**, *16*, 355S–363S.
- (6) Boskey, A. *Osteoporosis Int.* **2003**, *14*, S16–S20.
- (7) Yerramshetty, J. S.; Lind, C.; Akkus, O. *Bone* **2006**, *39*, 1236–1243.
- (8) Bradshaw, M. J.; Smith, M. L. *Acta Biomater.* **2014**, *10*, 1524–1531.
- (9) Rabe, M.; Verdes, D.; Seeger, S. *Adv. Colloid Interface Sci.* **2011**, *162*, 87–106.
- (10) Vogler, E. A. *Biomaterials* **2012**, *33*, 1201–1237.
- (11) Hunter, G. K.; O'Young, J.; Grohe, B.; Karttunen, M.; Goldberg, H. *Langmuir* **2010**, *26*, 18639–18646.
- (12) Hanein, D.; Geiger, B.; Addadi, L. *Langmuir* **1993**, *9*, 1058–1065.
- (13) Touryan, L. A.; Baneyx, G.; Vogel, V. *Colloids Surf., B* **2009**, *74*, 401–409.
- (14) Lee, M. H.; Ducheyne, P.; Lynch, L.; Boettiger, D.; Composto, R. J. *Biomaterials* **2006**, *27*, 1907–1916.
- (15) Nel, A. E.; Mädler, L.; Velegol, D.; Xia, T.; Hoek, E. M. V.; Somasundaran, P.; Klaessig, F.; Castranova, V.; Thompson, M. *Nature Mater.* **2009**, *8*, 543–557.
- (16) Hovgaard, M. B.; Rechendorff, K.; Chevallier, J.; Foss, M.; Besenbacher, F. *J. Phys. Chem. B* **2008**, *112*, 8241–8249.
- (17) Sang, L.-C.; Coppens, M.-O. *Phys. Chem. Chem. Phys.* **2011**, *13*, 6689–6698.
- (18) Elter, P.; Lange, R.; Beck, U. *Colloids Surf., B* **2012**, *40*, 139–146.
- (19) Azzopardi, P. V.; O'Young, J.; Lajoie, G.; Karttunen, M.; Goldberg, H. A.; Hunter, G. K. *PLoS One* **2010**, *5*, e9330.
- (20) Shen, J.-W.; Wu, T.; Wang, Q.; Pan, H.-H. *Biomaterials* **2008**, *29*, 513–532.
- (21) Liao, C.; Xie, Y.; Zhou, J. *RSC Adv.* **2014**, *4*, 15759.
- (22) Dolatshahi-Pirouz, A.; Jensen, T.; Foss, M.; Chevallier, J.; Besenbacher, F. *Langmuir* **2009**, *25*, 2971–2978.
- (23) Dolatshahi-Pirouz, A.; Jensen, T. H. L.; Kolind, K.; Bünger, C.; Kassem, M.; Foss, M.; Besenbacher, F. *Colloids Surf., B* **2011**, *84*, 18–25.
- (24) Donlon, L.; Nordin, D.; Frankel, D. *Soft Matter* **2012**, *8*, 9933.
- (25) Fernández-Montes Moraleda, B.; San Román, J.; Rodríguez-Lorenzo, L. M. *J. Biomed. Mater. Res., Part A* **2013**, *101*, 2332–2339.
- (26) Clause, K. C.; Barker, T. H. *Curr. Opin. Biotechnol.* **2013**, *24*, 830–833.
- (27) Singh, P.; Carraher, C.; Schwarzbauer, J. E. *Annu. Rev. Cell Dev. Biol.* **2010**, *26*, 397–419.
- (28) Dallas, S. L.; Chen, Q.; Sivakumar, P. *Curr. Top. Dev. Biol.* **2006**, *75*, 1–24.
- (29) Midwood, K. S.; Williams, L. V.; Schwarzbauer, J. E. *Int. J. Biochem. Cell Biol.* **2004**, *36*, 1031–1037.
- (30) Smith, M. L.; Gourdon, D.; Little, W. C.; Kubow, K. E.; Eguiluz, R. A.; Luna-Morris, S.; Vogel, V. *PLoS Biol.* **2007**, *5*, e268.
- (31) Wan, A. M. D.; Chandler, E. M.; Madhavan, M.; Infanger, D. W.; Ober, C. K.; Gourdon, D.; Malliaras, G. G.; Fischbach, C. *Biochim. Biophys. Acta* **2013**, *1830*, 4314–4320.
- (32) Akiyama, S. K.; Olden, K.; Yamada, K. M. *Cancer Metastasis Rev.* **1995**, *14*, 173–189.
- (33) Doostmohammadi, A.; Monshi, A.; Salehi, R.; Fathi, M. H.; Karbasi, S.; Pieles, U.; Daniels, A. U. *Mater. Chem. Phys.* **2012**, *132*, 446–452.
- (34) Baneyx, G.; Baugh, L.; Vogel, V. *Proc. Natl. Acad. Sci. U. S. A.* **2001**, *98*, 14464–14468.
- (35) Pathi, S. P.; Lin, D. D. W.; Dorvee, J. R.; Estroff, L. A.; Fischbach, C. *Biomaterials* **2011**, *32*, 5112–5122.
- (36) Weiner, S.; Bar-Yosef, O. *J. Archaeol. Sci.* **1990**, *17*, 187–196.
- (37) El Feki, H.; Rey, C.; Vignoles, M. *Calcif. Tissue Int.* **1991**, *49*, 269–274.
- (38) Zhao, W.; Xu, Z.; Yang, Y.; Sahai, N. *Langmuir* **2014**, *30*, 13283–13292.
- (39) Tooney, N. M.; Mosesson, M. W.; Amrani, D. L.; Hainfeld, J. F.; Wall, J. S. *J. Cell Biol.* **1983**, *97*, 1686–1692.
- (40) Baujard-Lamotte, L.; Noinville, S.; Goubard, F.; Marque, P.; Pauthe, E. *Colloids Surf., B* **2008**, *63*, 129–137.
- (41) Hull, J. R.; Tamura, G. S.; Castner, D. G. *Biophys. J.* **2007**, *93*, 2852–2860.
- (42) Berg, J. M.; Romoser, A.; Banerjee, N.; Zebda, R.; Sayes, C. M. *Nanotoxicology* **2009**, *3*, 276–283.
- (43) Meakin, P. *Nature* **1989**, *339*, 360–362.
- (44) Albanese, A.; Chan, W. *ACS Nano* **2011**, *5*, 5478–5489.
- (45) Cox, R. F.; Hernandez-Santana, A.; Ramdass, S.; McMahon, G.; Harmey, J. H.; Morgan, M. P. *Br. J. Cancer* **2012**, *106*, 525–537.
- (46) Pachman, L. M.; Veis, A.; Stock, S.; Abbott, K.; Vicari, F.; Patel, P.; Giczewski, D.; Webb, C.; Spevak, L.; Boskey, A. L. *Arthritis Rheum.* **2006**, *54*, 3345–3350.
- (47) Eidelman, N.; Boyde, A.; Bushby, A. J.; Howell, P. G. T.; Sun, J.; Newbury, D. E.; Miller, F. W.; Robey, P. G.; Rider, L. G. *Arthritis Res. Ther.* **2009**, *11*, R159.
- (48) Boettiger, D.; Ph, D. *Tissue Eng.* **1997**, *3*, 197–206.
- (49) Miller, T.; Boettiger, D. *Langmuir* **2003**, *19*, 1723–1729.
- (50) Vega, D.; Boettiger, D. *Mol. Biol. Cell* **1999**, *10*, 785–798.
- (51) Wang, K.; Andresen, E.; Eguiluz, R. C.; Wu, F.; Seo, B. R.; Fischbach, C.; Gourdon, D. *Biomaterials* **2015**, *54*, 63–71.
- (52) Wan, A. M.-D.; Inal, S.; Williams, T.; Wang, K.; Leleux, P.; Estevez, L.; Giannelis, E. P.; Fischbach, C.; Malliaras, G. G.; Gourdon, D. *J. Mater. Chem. B* **2015**, DOI: 10.1039/C5TB00390C.
- (53) Takamatsu, Y.; Simmons, P.; Moore, R.; Morris, H.; To, L.; Lévesque, J.-P. *Blood* **1998**, *92*, 3465–3474.
- (54) Mundy, G. R. *Nature Rev. Cancer* **2002**, *2*, 584–593.